nature communications

Article

https://doi.org/10.1038/s41467-026-70529-6

Magnetic-driven multifunctional optoelectronic catheter for in vivo chemical mapping and precisely guided-tumor therapy

Received: 9 January 2026

Accepted: 23 February 2026

Published online: 10 March 2026

Check for updates

Fuqian Chen[1], Xiaxu Liu[1], Yuanxi Zhang[1], Ying Zheng[1], Jingbo Yang[1,2], Tong Wu[1], Ke Zhao[1], Weiyuan Chen[1], Yuanyuan Li[1], Xia Gong[1], Hui Wang[3], Shuo Wu[1,3] ✉, Xi Xie[1,2] ✉ & Lelun Jiang[1] ✉

Precision tumor theranostic in minimally invasive interventions still face challenges such as poor navigational flexibility and limited functional integration. Here, we present a 2.5 mm magnetic-driven multifunctional optoelectronic catheter (MDMOC) fabricated via 3D multi-axis printing for in situ tumor mapping and therapy. The MDMOC integrates magnetic navigation, targeted drug delivery, localized photodynamic therapy, X-ray trackable imaging, and multiplexed biosensing of metabolites and ions. Its magneto-optical-electric-fluid multimodal design enables navigation through complex pathways, simultaneously monitoring biomarkers across the tumor microenvironment and delivering localized therapy. In rabbit and mouse tumor models, the MDMOC distinguished tumor from normal tissue, guided precise therapy, and minimized systemic side effects. In a Bama pig model, it achieved accurate navigation, multiparametric sensing, and targeted contrast agent delivery in complex anatomy. By integrating diagnostic and therapeutic functions with remote magnetic control, the MDMOC provides a versatile platform for real-time, precision-guided tumor diagnosis and therapy.

Tumors remain a major global health threat, and the development of precise diagnostic and efficient treatment technologies is crucial for both biomedical research and clinical application[1]. While conventional tumor diagnosis and treatment methods have achieved significant success in certain cases, they still face substantial challenges. For instance, tissue biopsies provide localized samples that may not fully reflect the tumor's distribution and characteristics throughout the body[2]. Meanwhile, the laborious process of sample handling, analysis, and treatment not only imposes psychological stress on patients but also prolongs the treatment cycle, ultimately affecting decisions and outcomes[3,4]. Uncertainty in tumor tissue boundaries increases the risk of residual lesions after surgical resection, raising the likelihood of recurrence and metastasis, negatively impacting prognosis[5–7]. Additionally, radiotherapy and chemotherapy lack the ability to accurately differentiate between normal and cancer cells, often causing severe systemic side effects and inducing resistance in tumor cells[8,9]. Furthermore, the heterogeneity of the tumor makes it difficult to achieve high-focus drug distribution within the tumor through systemic drug delivery, thereby reducing therapeutic efficacy[10–12]. Hence, an urgent need exists to develop more precise diagnostic and therapeutic

[1]Guangdong Provincial Key Laboratory of Sensor Technology and Biomedical Instrument, School of Biomedical Engineering, Shenzhen Campus of Sun Yat-Sen University, Shenzhen, China. [2]State Key Laboratory of Optoelectronic Materials and Technologies, Guangdong Province Key Laboratory of Display Material and Technology, School of Electronics and Information Technology, Sun Yat-Sen University, Guangzhou, China. [3]Department of Neurosurgery, Third Affiliated Hospital of Sun Yat-Sen University, Guangzhou, China. ✉e-mail: wush68@sysu.edu.cn; xiexi27@mail.sysu.edu.cn; jianglel@mail.sysu.edu.cn

methods or devices to address prolonged diagnostic cycles, difficulty in identifying tumor boundaries, and systemic side effects, thereby improving treatment outcomes and prognosis.

In recent years, the rapid advancement of minimally invasive interventional surgery has provided a promising pathway for enhancing the precision and efficiency of tumor targeting and therapy[13,14]. Catheter devices play a crucial role in these procedures, enabling both diagnosis and treatment through small incisions. However, conventional catheters rely heavily on operator expertise and are prone to low accuracy and instability. They require continuous X-ray imaging for real-time guidance, increasing radiation risks for both clinicians and patients[15,16]. Magnetically controlled catheters (MCC) have emerged as innovative interventional tools, offering remote control capabilities driven by an external magnetic field. These devices exhibit excellent navigational flexibility in complex anatomical environments such as blood vessels and the gastrointestinal tract[17–21]. Compared to traditional catheters, MCC reduce radiation exposure risk, improve precision of manipulation through machine assistance, and shorten treatment time, thereby enhancing patient safety and clinical efficiency[22–25]. As research progresses, MCC have shown immense potential across various clinical applications[26], including thrombectomy, drug delivery in narrow vessels[27–29], and targeted delivery or obstacle removal in regions including the gastrointestinal tract and cardiac chambers[30–33]. When integrated with optical flexible endoscopes[34–38] or optical coherence tomography (OCT) endoscopes[39], MCC enable high-resolution imaging in challenging areas, further improving procedure accuracy. However, current MCC are often limited to larger sizes or single functionalities due to the lack of suitable multimodal sensing components and advanced manufacturing technologies (Supplementary Table 1). In complex tumor surgeries, single-function catheters often fall short of diverse clinical needs, necessitating the use of multiple catheters, which increases procedural complexity and risk. Therefore, integrating multifunctionality while maintaining miniaturization and flexibility remains a key challenge.

Herein, we developed a magnetic-driven multifunctional optoelectronic catheter (MDMOC) for precisely-guided chemical mapping and in situ therapy in tumor surgery. The MDMOC, fabricated by 3D multi-axis printing technology, integrates the functionalities of remote magnetic navigation, real-time imaging guidance, in situ sensing, targeted drug delivery, and localized photodynamic therapy (PDT). Featuring a miniaturized design with a diameter of 2.5 mm, the MDMOC incorporates liquid metal-filled channels for enhanced flexibility and conductivity, built-in magnetic rings for real-time X-ray tracking of its trajectory, together with a hydrogel-coated surface to minimize tissue friction. The MDMOC integrates tumor mapping and therapeutic functions, with biosensors detecting multiple tumor-related biochemicals such as pH, hydrogen peroxide (H_2O_2), potassium ions (K^+), and glutathione (GSH) in real time to guide in situ treatment, thereby circumventing the delays inherent in traditional biopsy-to-treatment workflows. For multifocal or complex large tumors, magnetic navigation and precise in situ sensing allow effective exploration of tumor boundaries, reducing the risk of residual tumor tissue and preventing recurrence and metastasis. Target drug delivery combined with in situ PDT enables high-focus drug administration within the tumor and precise therapy, minimizing the risk of systemic side effects. Overall, the MDMOC provides a precise and efficient solution for tumor diagnosis and therapy, with its miniaturized design, remote controllability, and multifunctional integration offering promise for precision oncology.

Results

Therapeutic concept of MDMOC

The MDMOC effectively integrates magnetic navigation with real-time diagnostics and therapy, enabling precision-guided chemical mapping and in situ treatment of tumor lesions (Fig. 1). Under real-time CT or digital subtraction angiography (DSA) imaging guidance, physicians can remotely control the MDMOC to navigate through complex in vivo environments and reach target lesions using a magnetic field manipulation system (e.g., magnet-equipped robotic arm system) (Fig. 1A). This approach substantially reduces physician exposure to X-ray radiation, a common concern in conventional interventional therapies. Equipped with four multimodal electrochemical biosensors, the MDMOC enables real-time monitoring of key biochemical markers associated with the tumor microenvironment, including pH, H_2O_2, K^+, and GSH (Fig. 1B, C). These markers reflect abnormal metabolic activity and facilitate the differentiation between tumor and normal tissues[40–44]. Leveraging its capabilities in magnetic navigation, tissue penetration, and spatially distributed multi-point sensing, the MDMOC can investigate suspected lesions across multiple anatomical sites, accurately delineate tumor margins and spatial distribution patterns, and support personalized interventional strategies.

In terms of therapeutic functionality, the MDMOC incorporates internal channels for localized and precise drug administration, ensuring high-concentration intratumoral drug while minimizing systemic toxicity (Fig. 1C). Integrated optical fiber further enables efficient in situ PDT, addressing the limitations of conventional PDT for deep-seated tumors due to light attenuation and limited tissue penetration. By combining localized drug delivery, in situ PDT, and real-time biochemical guidance in a single catheter, the MDMOC enables adaptive therapy that responds directly to intraoperative data rather than relying on preoperative assumptions. Specifically, for multifocal or large tumor masses with complex spatial distributions, the MDMOC ensures comprehensive tumor coverage, delivering highly targeted and efficient therapeutic solutions. This in situ therapeutic approach not only enhances treatment precision but also minimizes collateral damage to surrounding healthy tissues. Additionally, the MDMOC exhibits excellent magnetic responsiveness and flexibility, allowing for agile and controllable navigation under magnetic actuation (Fig. 1D and Supplementary Fig. 1). Moreover, the MDMOC was mainly integrated with a polymer head, four electrochemical sensors, two magnetic rings, and two flexible multi-axial sheaths (Fig. 1E and Supplementary Fig. 2). Its miniaturized and compact design allows for minimally invasive access through a small incision, significantly reducing patient trauma. Compared with existing MCC (Supplementary Table 1), the MDMOC demonstrates significant advantages in remote controllability, diagnostic precision, and multimodal therapeutic integration, highlighting its clinical potential in tumor diagnosis and treatment.

Assembly of MDMOC

The MDMOC is primarily composed of a polymer head, four biosensors, two magnetic rings, and two multi-axial sheaths, all of which are strongly bonded together using biocompatible UV-curable resin (Fig. 2A, B and Supplementary Fig. 3). The MDMOC features a compact design with a maximum diameter of 2.5 mm, making it compatible with minimally invasive procedures. The arrow-shaped polymer head with a sharp tip (tip diameter of ~10 μm) consists of diamond-shaped pores that enable efficient fluid and agent flow while maintaining mechanical strength at the catheter tip (Fig. 2C). The sensing ends of biosensor electrodes are exposed within the inner cavity of the polymer head, effectively protecting them from direct friction with surrounding tissues while allowing target fluids to flow through the diamond-shaped pores for analysis (Fig. 2D and Supplementary Fig. 4). The other ends of biosensor electrodes are inserted through the designated channels of the multi-axial sheath A. The arrow-shaped head (Supplementary Fig. 5) can be interchangeably replaced with a round-shaped head (Supplementary Fig. 6), thereby expanding its versatility for various clinical applications. This modularity allows adaptation to different vascular anatomies and procedural requirements, enhancing clinical

https://doi.org/10.1038/s41467-026-70529-6

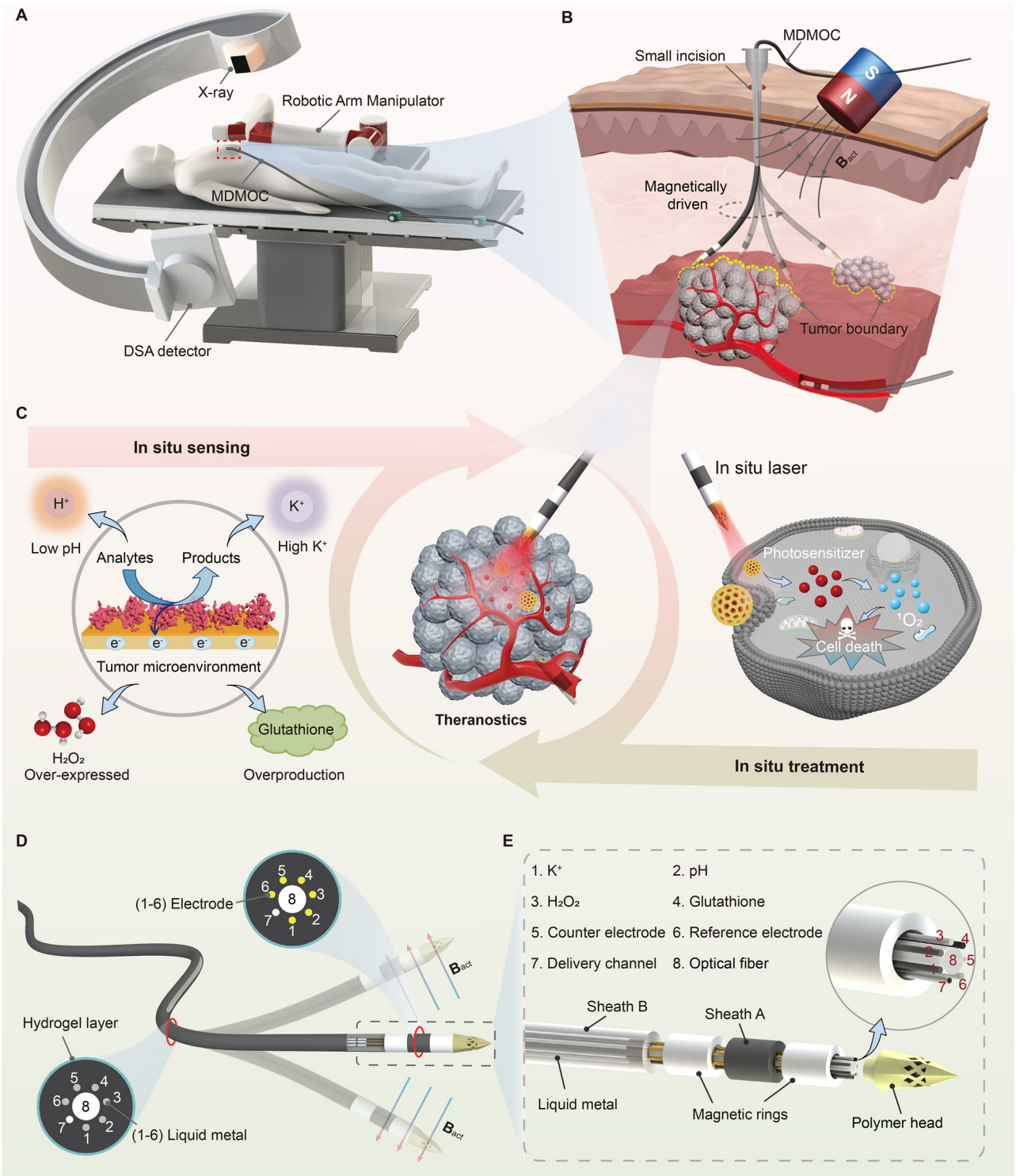

Fig. 1 | Schematic illustration of MDMOC for tumor diagnosis and therapy. **A** Overview of the clinical application of MDMOC. The MDMOC is precisely navigated using a magnet-equipped robotic arm system under real-time DSA imaging guidance, enabling the diagnosis and treatment of suspected tumor lesions at multiple sites. **B** Integration of multimodal electrochemical biosensors with flexible magnetic navigation enables accurate identification of tumor boundaries and analysis of spatial distribution. **C** Mechanism of integrated diagnosis and therapy at the tumor sites using the MDMOC, which features multimodal electrochemical biosensing and enhanced in situ PDT. **D** The MDMOC exhibits excellent magnetic responsiveness and flexibility, allowing agile magnetic navigation. **E** Illustration of the main components of the MDMOC.

utility. Notably, the flexible multi-axial sheath channels not only facilitate the delivery of therapeutic or contrast agents but also enable the cleaning of biosensors with saline or PBS in case of potential contamination. Additionally, the magnetic rings exhibit an axial magnetization direction aligned with the catheter axis, ensuring stable magnetic actuation (Fig. 2E), which is critical for precise catheter navigation and positioning within complex vascular environments.

We developed a 3D printer equipped with a multi-core coaxial nozzle for the fabrication of multi-axial sheaths (Supplementary Fig. 7). The multi-nozzle consists of a large outer nozzle and eight smaller

https://doi.org/10.1038/s41467-026-70529-6

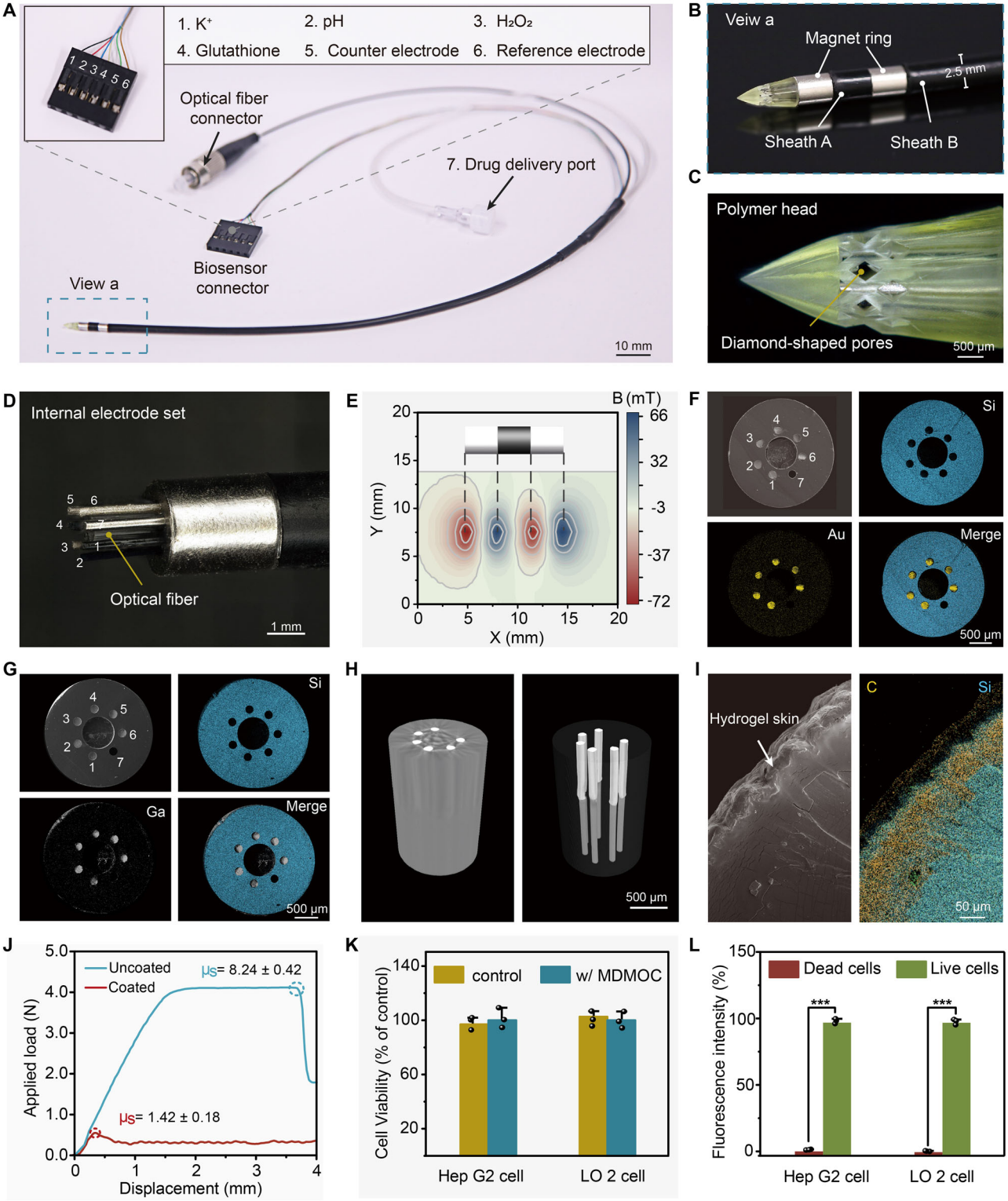

Fig. 2 | Assembly and characterization of MDMOC. A Optical image of MDMOC, which was the integration of a polymer head, four electrochemical biosensors, two magnetic rings, two multi-axial sheaths, and corresponding adapters. **B** Optical image of the MDMOC head. **C** Optical image of the polymer head. $n = 5$ independent experiments. **D** Optical image of electrochemical biosensors, including four working electrodes for K^+, pH, H_2O_2, and GSH sensing, as well as a reference electrode and a counter electrode. **E** Magnetic field distribution of the magnetic rings. **F**, **G** SEM and elemental maps of Au wire-filled sheath A and liquid metal-filled sheath B. $n = 3$ independent experiments. **H** Micro-CT image of the connections between Au electrode wires and liquid metal channels as conductors within the MDMOC. **I** SEM image of the modified hydrogel surface on the MDMOC and its corresponding elemental distribution. $n = 3$ independent experiments. **J** Surface friction coefficients before and after hydrogel coating. **K** Cytotoxicity evaluation of the MDMOC. Data are shown as mean ± s.d. $n = 3$ independent biological experiments. **L** Toxicity validation of the MDMOC using live/dead cell staining. Data are shown as mean ± s.d. $n = 3$ independent biological experiments. $P = 0.00013$ for HepG2 cells and $P = 0.00012$ for LO2 cells versus control.

internal nozzles, each connected to separate syringes containing air, PDMS, or liquid metal. This design allows for the simultaneous extrusion of air, PDMS, and liquid metal through the multi-nozzle, enabling the direct printing of multi-axial sheaths in one step. The printed multi-axial sheaths are cured at 70 °C for 1 h. This 3D printing approach offers design flexibility and significantly improves manufacturing efficiency. The multi-axial sheath A includes eight empty channels, six of which are inserted with electrodes: four working electrodes for K^+, pH, H_2O_2, and GSH sensing, as well as a reference electrode and a counter electrode. Au wires serve as the base material for these electrodes. The elemental distribution of Au wire within six smaller channels of multi-axial sheath A can be observed (Fig. 2F and Supplementary Fig. 8). These Au wires are inserted through the designated channels of multi-axial sheath A and electrically connected with liquid metals within channels of the multi-axial sheath B. The Ga elemental distribution of liquid metal within channels of multi-axial sheath B is also visible (Fig. 2G and Supplementary Fig. 8). Furthermore, the robust bonding between the base electrodes and the liquid metals for electrical conduction is confirmed using Micro-CT imaging (Fig. 2H). An optical fiber with a diameter of 750 μm for light transmission is inserted through the larger inner channel of multi-axial sheath A and B, as shown in Fig. 2G, H. Therefore, the MDMOC is successfully constructed, which integrates with the biosensors for in situ detection, an optical fiber for PDT, and an empty channel for drug delivery. To demonstrate its suitability for deep vascular interventional applications, a 1-meter-long MDMOC catheter with a round polymer head could also be fabricated (Supplementary Fig. 9).

To minimize the friction between MDMOC and surrounding tissue or blood vessel wall, as well as to enhance its biocompatibility, a hydrogel layer (~25 μm thick) was in situ formed on the catheter surface via UV-induced crosslinking of N,N-dimethylacrylamide (DMAA) and Irgacure-2959 (Fig. 2I and Supplementary Fig. 10). In addition, a PDMS skin was coated on the surfaces of the magnetic rings to improve biocompatibility and prevent direct exposure (Supplementary Fig. 11). The static friction coefficients of the catheter surface, both with and without the hydrogel layer, were measured (Fig. 2J and Supplementary Fig. 12). The introduction of the hydrogel coating significantly reduced the static friction coefficient from 8.24 ± 0.42 to 1.42 ± 0.18. This significant reduction in friction is expected to improve catheter navigation and lower the risk of vascular injury during interventions. The cytotoxicity of MDMOC was assessed using live/dead cell viability assays and CCK-8 assays (Fig. 2K, L and Supplementary Fig. 13). The results showed no significant toxicity, with cell viability comparable to the control group. According to the USP (ISO 10993-5) standard (≥70% viability), the MDMOC exhibits excellent biocompatibility, making it suitable for interventional therapies.

Magnetic, optic, electric, and drug delivery performance of MDMOC

The bending deformation of the MDMOC under magnetic actuation was investigated (Fig. 3, Supplementary Figs. 14 and 15). An actuating magnetic field $\mathbf{B}_{act}$ was applied to the MDMOC, resulting in rapid bending due to the induced magnetic torque T_m between the actuating field and the two magnetic rings: $T_m = \mu_0(\mathbf{M}\times\mathbf{B}_{act})$, where $\mathbf{M}$ is remnant magnetization of the magnetic rings and μ_0 is the magnetic permeability of free space (Fig. 3A). According to the principle of minimum potential energy, the MDMOC tends to align the its magnetization vector $\mathbf{M}$ along the direction of actuating field $\mathbf{B}_{act}$, thereby generating a magnetic torque T_m that induces bending. As the bending angle θ increases, the magnetic torque T_m decreases, while the elastic torque $T_e = E\bullet Id\theta/ds$ increases, where E is the Young's modulus, I is the area moment of inertia, and s is the arc length coordinate[45]. Eventually, equilibrium is established when $T_m = T_e$, achieving a dynamic balance between magnetic and elastic torques. Finite element simulations confirmed that the MDMOC bends to align with the actuating field (Fig. 3B). Moreover, MDMOCs with micro-channels filled with liquid metal, copper wire, and air (hollow) were fabricated and tested under a 200 mT vertical magnetic field. Experimental bending angles agreed well with simulations (Fig. 3C and Supplementary Fig. S16). The liquid metal-filled MDMOC achieved a maximum bending angle of approximately 51° ± 0.5°, 8.2 times greater than the copper-wire-filled version, highlighting its superior flexibility. The bending elastic modulus of liquid metal-filled MDMOC is very close to that of the air-filled MDMOC and is only one-fifth that of the copper-wire-filled MDMOC (Fig. 3D). This superior deformability stems from the fluid nature of liquid metal, which enables significant bending without compromising electrical conductivity (Supplementary Fig. S17), thereby facilitating precise magnetic navigation and reliable sensing in complex clinical environments.

The MDMOC head can smoothly maneuver along a pre-designed path and transmit a laser via its optical fiber to illuminate the photochromic pattern "SYSU" within 39 s under magnetic actuation, using a self-developed 8-axis electromagnetic coil apparatus (Fig. 3E, F, Supplementary Fig. 18, and Supplementary Movie 1). This demonstration confirms precise directional control and effective laser delivery, essential for targeted PDT and multi-lesion exploration. Furthermore, six LEDs connected via a custom PCB verified the electrical connections of each channel (Supplementary Fig. 19). The MDMOC accurately navigated to sequentially illuminate all six LEDs within 40 s under magnetic actuation (Fig. 3G, H, Supplementary Movie 1), demonstrating interference-free electrical conductivity and reliable multi-site in situ electrochemical tumor sensing.

Penetration and fracture performance are crucial for in situ biosensing and drug delivery. The MDMOC effectively punctured an agarose gel tissue model and delivered drug solution (Supplementary Fig. 20). Penetration performance was further investigated in ex vivo liver tissue (Fig. 3I). The insertion force rose rapidly upon initial contact with the liver surface, followed by a steady increase. At point "P," the insertion force suddenly drops, then increases again as the MDMOC penetrates deeper. This abrupt drop at point "P" represents the critical penetration force[46,47], as measured to be ~0.22 N. The resulting puncture hole in the liver tissue is observed in the inset of Fig. 3I and Supplementary Fig. 21, confirming successful tissue penetration. The fracture performance of the MDMOC was investigated by vertically compressing its tip against an aluminum (Al) plate. The compression force gradually increases with the loading displacement. At a compression force of approximately 2 N (Fig. 3J), no buckling of the MDMOC is observed. This compression force is significantly higher than the critical penetration force, indicating sufficient mechanical robustness to penetrate tissue safely during procedures. The MDMOC stably delivered liquid drug at a pre-set flow rate with only 3.78% deviation under different bending angles using a peristaltic pump (Fig. 3K, Supplementary Fig. 22). To ensure precise administration, Rhodamine B-filled MDMOC was swayed for 1 h, showing no drug leakage, confirming the integrity of drug delivery channel (Fig. 3L).

In vitro electrochemical sensing performance of MDMOC

The smooth Au-based electrodes were roughened and cleaned to produce a textured surface (Supplementary Fig. 23), to aid subsequent functionalization. The functionalized electrodes exhibited fibrous and nanostructured morphologies (Fig. 4A). For the pH electrode, polyaniline (PANI) was electrodeposited onto the Au-based electrode, forming an interwoven PANI fiber structure. The deprotonation properties of PANI enable a sensitive response to pH changes, thus facilitating pH detection[48,49]. For the platinum-functionalized electrode, Pt nanoparticles serve as efficient catalysts for the redox reactions of hydrogen peroxide, thereby promoting electron transfer and enabling highly sensitive and selective hydrogen peroxide detection[50,51]. The potassium ion (K^+) electrode is coated with a K^+-selective polymer membrane (Supplementary Fig. 24), which allows

https://doi.org/10.1038/s41467-026-70529-6

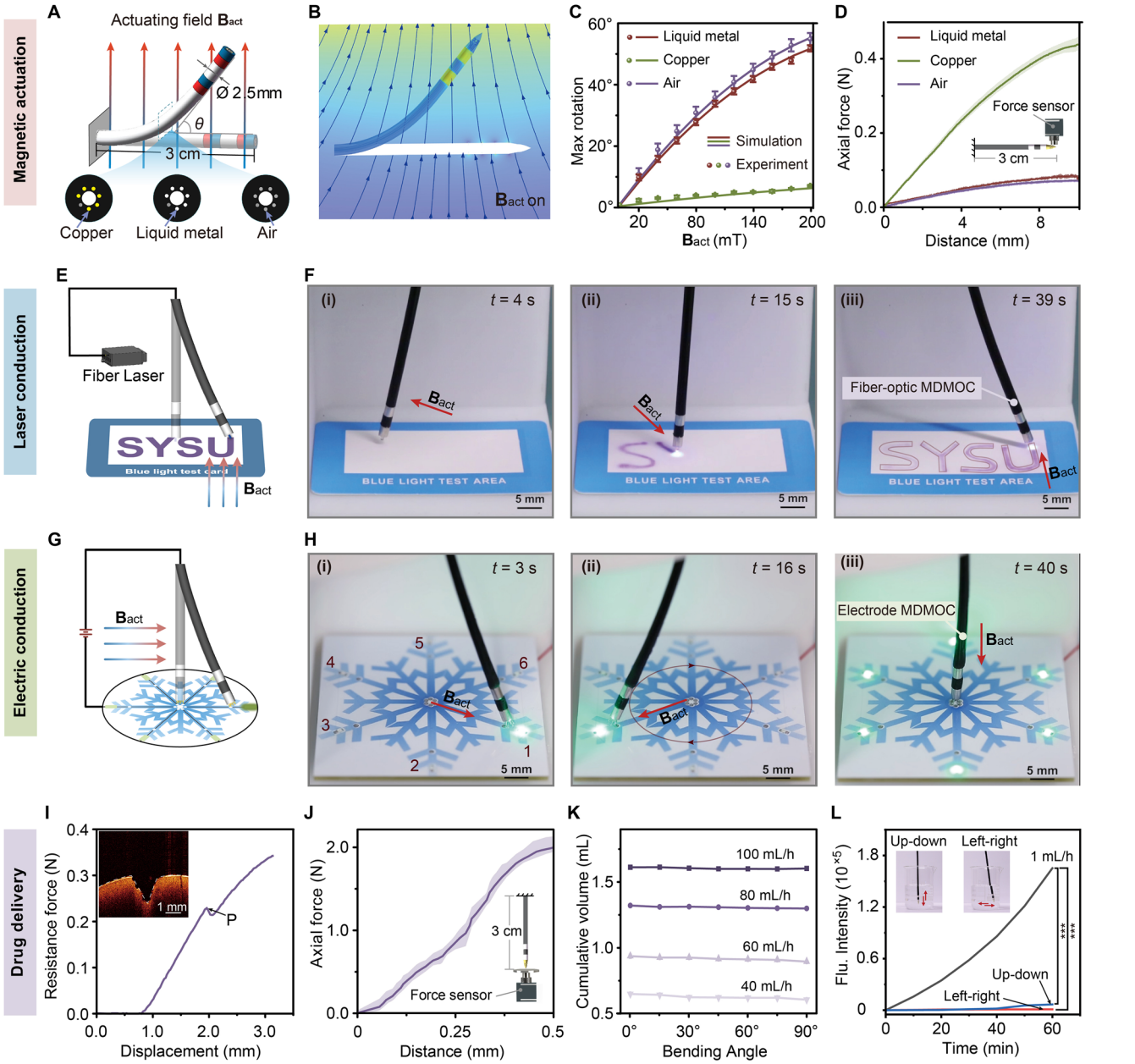

Fig. 3 | Magnetic, optic, electric, and drug delivery performance of the MDMOC. **A** Schematic illustration and **B** finite element analysis of magnetically-actuated deformation under an external magnetic field applied perpendicular to the MDMOC. **C** Bending angles of MDMOC, with its micro-channels filled with air, liquid metal, and copper wires, actuated by magnetic fields ranging from 0 to 200 mT. Data are shown as mean ± s.d. $n = 3$ independent device-level experiments. **D** Lateral force applied on the MDMOC head with its micro-channels filled with air, liquid metal, and copper wires. Data are shown as mean ± s.d. $n = 3$ independent device-level experiments. **E** Schematic illustration and **F** demonstration of the MDMOC maneuvering along a pre-designed path and transmitting a laser to activate a photochromic pattern of "SYSU" under magnetic actuation. **G** Schematic illustration and **H** demonstration of the MDMOC maneuvering to target sites to illuminate LEDs under magnetic actuation. **I** The penetration force of the MDMOC into liver tissue. Inset: the OCT image of puncture hole in liver tissue. **J** The fracture force of the MDMOC when compressed against an Al plate. Data are shown as mean ± s.d. $n = 3$ independent device-level experiments. **K** Effect of bending angles on the delivery rate of liquid drugs using MDMOC. **L** Drug leakage evaluation of the MDMOC during 1 h of up-and-down and left-and-right swaying, compared with continuous drug delivery at a rate of 1 mL/h. Data are shown as mean ± s.d. $n = 3$ independent device-level experiments. Exact P values: 1 mL/h vs up-down = 4.87×10^{-6}; 1 mL/h vs left-right = 6.42×10^{-6}.

the potassium ion concentration to substantially modulate the surface charge, thereby enabling precise K^+ detection[52,53]. The GSH electrode is modified with CoPcs-PEDOT nanostructures, where cobalt phthalocyanine (CoPcs) efficiently catalyzes the reactions of thiol group in GSH molecules, thereby enabling highly sensitive GSH detection[54,55]. Energy dispersive spectrometer (EDS) elemental analysis was performed to validate surface functionalization (Supplementary Fig. 25). Significant enrichment of characteristic elements, such as silver (Ag), platinum (Pt), oxygen (O), and sulfur (S), can be observed, thereby confirming effective modification of each functional layer.

In vitro electrochemical sensing performance of MDMOC was systematically evaluated (Fig. 4 and Supplementary Fig. 26). The pH electrode exhibits a stepwise potential signal response over a broad pH range of 3–9 (Supplementary Fig. 27), which effectively encompassing the physiologically relevant tumor microenvironment pH range (6.5–6.8)[56]. To further validate its applicability for detecting subtle pH

https://doi.org/10.1038/s41467-026-70529-6

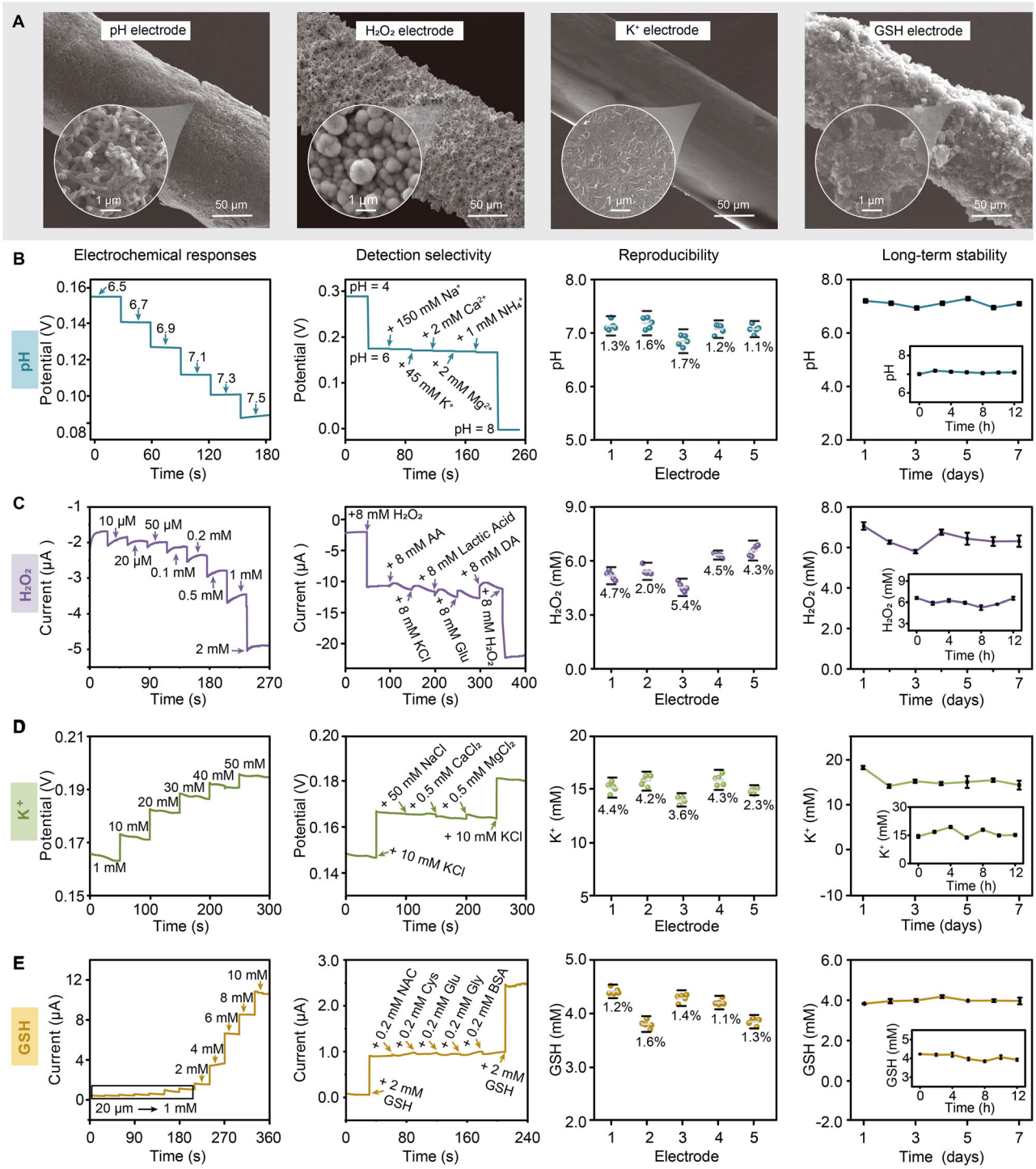

Fig. 4 | In vitro electrochemical sensing performance of the MDMOC. A SEM images of the pH, H_2O_2, K^+, and GSH sensing electrodes. Sensing performance of each type of electrode: **B** pH electrode, **C** H_2O_2 electrode, **D** K^+ electrode, and **E** GSH electrode. The sensitivity, selectivity, reproducibility, and long-term stability of each electrode were evaluated. Data are shown as mean ± s.d. $n = 3$ independent experiments for each electrode.

variations in the tumor microenvironment, the detection range was refined to pH 6.5–7.5, yielding a linear potential–pH relationship with a sensitivity of 66.2 mV/pH and a correlation coefficient of 0.99 (Fig. 4B). To evaluate anti-interference performance, several commonly occurring positively charged ions (K^+, Na^+, Ca^{2+}, Mg^{2+}, and NH_4^+) were introduced. The responses to these interferents were negligible, indicating excellent anti-interference capability of the pH electrode. For reproducibility, the response trends and sensitivities across different electrode batches are consistent, with a relative standard deviation (RSD) of only 1.37%. Additionally, long-term stability studies show that the measured potential signal remains within 95–105% of the initial values, demonstrating stable pH response for at least 1 week.

For the H_2O_2 electrode, the current signal (absolute value) exhibits a concentration-dependent response with increasing H_2O_2 concentrations, with a sensitivity of 1.584 μA/mM and a correlation coefficient of 0.99 (Fig. 4C, Supplementary Fig. 27). In terms of

selectivity, the minimum and maximum interference signals from various interferents are approximately 0.92 and 5.20%, respectively, indicating excellent selectivity. For reproducibility, the RSD of the current signals from different batches of electrodes for 6 mM H_2O_2 is only 4.19%, with consistent detection trends and sensitivities observed. For long-term stability, the amperometric signals of the H_2O_2 electrode remain stable within 85–110% of the initial values, demonstrating reliable long-term performance.

For the K^+ electrode, the measured potential signal exhibits a concentration-dependent stepwise change, with a sensitivity of 1 mV/mM and a correlation coefficient of 0.998 (Fig. 4D and Supplementary Fig. 27). In terms of selectivity, the maximum interference signal from any interferent is approximately 1.63%. Reproducibility and long-term stability studies show that the RSD for measurements of 15 mM K^+ across different batches of electrodes is 3.79%, and the potential response signal remained within 90–110% of the initial value, indicating good reproducibility and stability. For the GSH electrode, chronoamperometry at a potential of 0.4 V was used to record the amperometric response, which increases stepwise with glutathione concentrations and shows a linear relationship with a sensitivity of 0.89 μA/mM and a correlation coefficient of 0.998 (Fig. 4E and Supplementary Fig. 27). Interference tests were conducted by adding substances such as bovine serum albumin (BSA) and cysteine, confirming that signal disturbance could be ignored. Reproducibility was evaluated by recording the amperometric signals of five GSH electrodes, resulting in an RSD of only 1.29%. The amperometric response of the same electrode consistently remains within 95–105% of the initial measurement, demonstrating reliable reproducibility and long-term stability. To improve detection accuracy in real tissue environments, a first-order correction algorithm (Supplementary Fig. 28) was implemented to eliminate pH-induced interference in the H_2O_2, K^+, and GSH electrodes, significantly improving signal stability and accuracy under physiological conditions. Meanwhile, the mechanical reliability of MDMOC was evaluated under dynamic conditions, including liquid flow and bending (Supplementary Fig. 29). All four sensors maintained stable sensing performance during the tests. Notably, the excellent conductivity and fluidity of the liquid metal minimized signal fluctuations during navigation, ensuring consistency and accuracy of real-time detection.

Reversibility testing is a critical factor in distinguishing tumor tissues from normal tissues at multiple lesion sites. Therefore, the reversibility of each electrode in response to changes in analyte concentrations was investigated. The results demonstrate significant sensitivity to variations in target analyte concentrations for all electrodes. Overall, the MDMOC sensing electrodes demonstrate excellent sensitivity, good selectivity, reliable reproducibility, and long-term stability for target analyte detection. The capability to reversibly change signals in response to varying concentration environments allows for the effective differentiation of biomarker concentration levels between tumor tissues and normal tissues (Supplementary Fig. 30), thereby enabling precise tumor diagnosis.

In vivo investigation of MDMOC for tumor-related chemical mapping

Precise intraoperative delineation of tumor margins is essential for achieving individualized resection and targeted therapy. The detection accuracy and clinical feasibility of MDMOC in various boundary scenarios using a rabbit orthotopic hepatic tumor model were evaluated. The combined schematic (Fig. 5A) depicts minimally invasive transabdominal insertion under magnetic actuation and the integrated closed-loop workflow, in which magnetic navigation rapidly targets the suspected lesion, in situ sensing verifies lesion characteristics, and subsequent PDT or drug release is initiated without delay. The multipoint biochemical mapping defines lesion boundaries, directly controlling treatment time and location to ensure that treatment is applied only to the confirmed lesion area. The intraoperative procedure employed a robotic arm equipped with a magnet and guided by vision assistance to achieve stable catheter positioning. Real-time imaging indicated that the interval from navigation to treatment initiation was ~260 s, representing a substantial reduction compared with conventional stepwise diagnosis and intervention workflows and minimizing the influence of lesion status changes during the therapeutic window (Fig. 5B). The sensing-guided integration of diagnosis and therapy is pivotal for reducing uncertainties arising from dynamic alterations in lesion characteristics.

To assess the advantage of multimodal fusion in mapping complex boundaries, we used four biochemical sensors (pH, H_2O_2, K^+, and GSH) for multi-point detection. Heatmaps revealed steep and consistent concentration gradients across the tumor–normal interface for all analytes, with contour lines corresponding to the inferred boundaries (Fig. 5C). Multimodal fusion further enhanced signal contrast and boundary continuity (Fig. 5D), reducing the variability associated with single-analyte measurements. Compared to ultrasound (Fig. 5E) and histopathology (Fig. 5F), the fused results showed better positional concordance than single-channel methods. Quantitative analysis showed that the tumor recall rate reached 100%, indicating that the detected boundaries fully encompassed the true tumor area. The Fréchet distance, calculated between the detected boundary and the histopathological standard, was the smallest for the fused approach at 2.11 mm, reflecting superior alignment with the pathological margin (Fig. 5G). The fusion strategy proved effective not only for multifocal lesions but also for solitary tumors (Supplementary Fig. 31) and partial boundaries of larger masses. Local heatmaps from single sensors captured fine edge variations (Fig. 5H), while fusion maps provided more continuous tumor signals and better boundary concordance (Fig. 5I). Compared with ultrasound (Fig. 5J) and gross optical images (Fig. 5K), the fusion maps matched the ultrasonic standards more closely. Statistical analysis confirmed complete tumor coverage within the fused boundaries, with a tumor recall rate of 100% and a Fréchet distance of 2.62 mm, demonstrating that the approach maintains high precision and robustness for both localized and multifocal boundary mapping (Fig. 5L). Notably, this performance was achieved in the complex intraoperative biological environment, where blood, interstitial fluid, and heterogeneous tissues typically challenge sensor stability and specificity. The consistent in vivo gradients and boundary concordance demonstrate MDMOC's high signal fidelity and resistance to matrix interference, supporting its robustness for real-time surgery.

Furthermore, the spatial resolution of MDMOC was quantitatively assessed using an in vitro agarose gradient model (Supplementary Fig. 32) combined with Boltzmann sigmoid fitting and a multi-sensor gradient fusion algorithm. The optimal single-channel resolution was 1.69 mm, while four-channel fusion improved it to 0.49 mm, achieving sub-millimeter precision. Although tissue deformation and fluid dynamics may slightly reduce performance, MDMOC achieved millimeter-level accuracy in animal models, approaching histopathological standards. In summary, MDMOC consistently detected multifocal, solitary, and localized tumor boundaries with high accuracy and resolution (Supplementary Fig. 33). The multimodal fusion strategy effectively corrected boundary errors caused by the variability or background noise of single biomarkers, improving the reliability of margin detection. More importantly, the system enables a fast "sensing–decision–therapy" closed-loop workflow during surgery, significantly reducing operation time and the need for repeat procedures. Noted that this unique system integrates a coordinated set of functions, combining controllable magnetic actuation with tumor boundary mapping. MDMOC achieves millimeter-to-sub-millimeter spatial resolution while maintaining stable sensing performance in physiologically relevant environments. This work not only provides a

https://doi.org/10.1038/s41467-026-70529-6

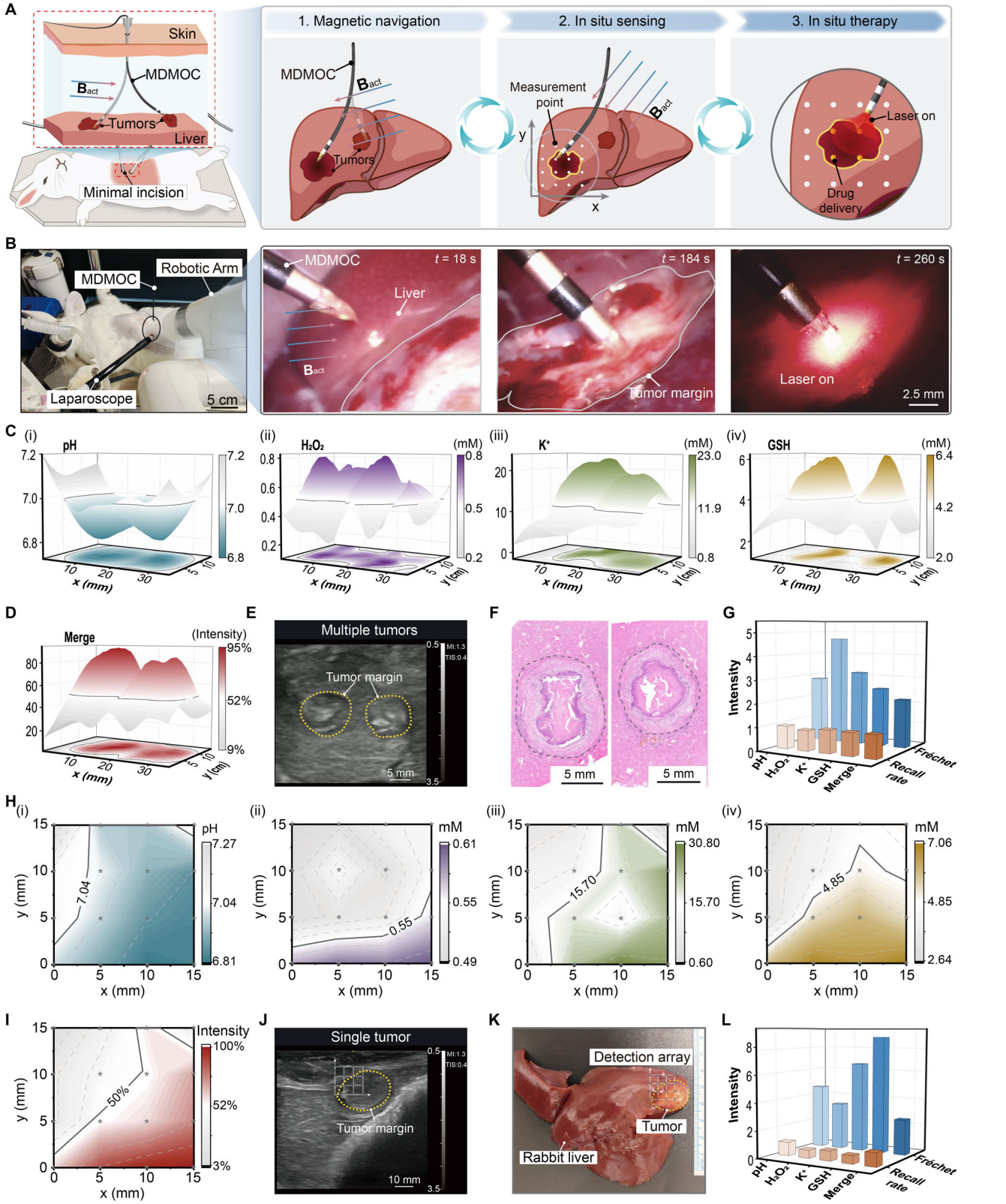

Fig. 5 | In vivo evaluation of MDMOC for tumor-related chemical mapping. **A** Schematic of minimally invasive transabdominal insertion under magnetic actuation and closed-loop workflow integrating navigation, in situ sensing, and on-demand therapy. **B** Intraoperative setup with magnet-equipped robotic arm and vision-assisted guidance, achieving navigation-to-treatment initiation within ~260 s. **C** Spatial heatmaps showing in situ multifocal detection of four biomarker concentrations (pH, H_2O_2, K^+, and GSH). Concentration heatmap generated by spatial interpolation of discrete measurements. **D** Multimodal fusion heatmap of the four biosensors. **E** Ultrasound image of multifocal liver tumors. **F** H&E-stained histological section of multifocal tumors. $n = 3$ independent experiments. **G** Comparison of tumor boundaries derived from single-sensor data, multi-sensor fusion, and histology. **H** Spatial heatmaps of biomarker concentration in situ sensing around the peripheral region of a single tumor. **I** Fusion heatmap showing tumor margin detection using all four sensors. **J** Ultrasound image of a single tumor. **K** Photograph of the rabbit liver with tumor. **L** Comparison of the detected tumor margin with histological result.

solution for precise oncologic margin assessment but also paves the way for future AI-driven real-time surgical navigation.

In vivo sensing and therapeutic performance of MDMOC in rats

We prepared poly (lactic-co-glycolic acid)-encapsulated chlorin e6 (PLGA@Ce6) photosensitizer-loaded nanoparticles for MDMOC-mediated PDT for in vivo treatment (Supplementary Fig. 34)[57,58]. Their cellular uptake and PDT efficacy were confirmed in vitro (Supplementary Figs. 35 and 36). Compared to conventional PDT, MDMOC-mediated PDT generated significantly higher reactive oxygen species in deep tissues with much lower drug doses[59]. Moreover, fluorescence imaging of liver tissue showed that local PLGA@Ce6 delivery via MDMOC resulted in markedly greater intratumoral accumulation than systemic administration through tail vein injection (Supplementary Fig. 37), highlighting the advantage of targeted delivery in reducing dosage and minimizing off-target effects. We further established an orthotopic liver cancer mouse model to evaluate the in vivo sensing and therapeutic performance of the MDMOC. In vivo anti-tumor experimental design and the operation process of MDMOC-mediated PDT in tumor-bearing mice are illustrated in Fig. 6A and Supplementary Fig. 38. In situ electrochemical measurements were performed by inserting the MDMOC into either liver tumors or normal tissues (Fig. 6B). Subsequently, tissue regions were excised, and interstitial fluid was extracted for quantitative analysis using standard analytical instruments as a reference. Electrical signals from MDMOC were converted to concentrations using a calibration curve. Statistical analysis of MDMOC results and reference values was visualized as heatmaps (Fig. 6C). The results show a significant positive difference between tumor and normal tissues for both methods. Moreover, MDMOC measurements exhibit strong agreement with the results obtained from standard instruments. For instance, changes in analytes detected in tumor tissue, including decreased pH and elevated concentrations of H_2O_2, K^+, and GSH, are consistent with the tumor microenvironment characteristics. Error grid analysis was used to evaluate the accuracy and reliability of MDMOC. The results showed that over 80.5% of MDMOC data points fell within zones A and B, indicating that most in vivo measurements were consistent with values detected by laboratory standard instruments, demonstrating the high accuracy and clinical reliability of MDMOC (Supplementary Figs. 39 and 40).

To systematically evaluate the therapeutic efficacy of each group, multiple indicators were employed, including periodic monitoring of mouse body weight (Fig. 6D), changes in fluorescence intensity at the tumor site (Fig. 6E and Supplementary Fig. 41) and survival rates throughout the treatment cycle (Fig. 6F). The results demonstrated no significant changes in body weight across all groups over the 15-day treatment period, suggesting that the therapeutic protocols did not induce noticeable systemic toxicity. In terms of changes in tumor fluorescence intensity, the control group exhibited a gradual increase in fluorescence, reflecting continuous tumor progression. By contrast, both the transdermal group and the MDMOC group displayed a significant reduction in tumor fluorescence intensity, indicating effective inhibition of tumor growth. Notably, the MDMOC group exhibited the most pronounced inhibitory effect. To further validate the therapeutic efficacy, tumor tissues from each group were excised and analyzed post-treatment. Optical imaging results revealed that the tumor volumes of the MDMOC group were significantly smaller compared to the other two groups, confirming its superior anti-tumor performance (Fig. 6G and Supplementary Fig. 42). This observation was consistent with the fluorescence measurements, underscoring the therapeutic advantage of MDMOC. Additionally, histological analyses, including hematoxylin and eosin (H&E) staining, terminal deoxynucleotidyl transferase dUTP nick-end labeling (TUNEL) staining, and Ki67 immunohistochemistry, were conducted on liver tumor tissues (Fig. 6H). H&E staining of major organs revealed no observable tissue damage, indicating minimal systemic toxicity (Supplementary Fig. 43). H&E staining revealed that tumor tissues in the MDMOC group exhibited significant pathological alterations, with a marked reduction in tumor cell density (Fig. 6I). TUNEL staining analysis (Fig. 6J) further confirmed that the MDMOC group showed the highest proportion of tumor necrosis and late-stage apoptosis, indicating the highest level of tumor cell apoptosis among all groups ($p < 0.001$). Meanwhile, Ki67 immunohistochemical staining (Fig. 6K) demonstrated a significant decrease in the expression of proliferative markers in the MDMOC group, suggesting that MDMOC not only effectively induces tumor cell apoptosis but also substantially inhibits tumor cell proliferation. Furthermore, the surgical site following two minimally invasive MDMOC treatments revealed excellent wound healing with minimal tissue damage (Supplementary Fig. 44), confirming its suitability for repeated minimally invasive procedures. Overall, MDMOC enables real-time, in situ electrochemical biosensing to accurately distinguish tumor boundaries from normal tissue, while simultaneously facilitating targeted drug delivery and in situ PDT.

In vivo minimally interventional surgery of MDMOC in pigs

We further validated the clinical potential of MDMOC in Bama pigs through in vivo interventional procedures (Fig. 7A). The intravascular trajectory of MDMOC was recorded in real-time using DSA. In vascular interventional applications, MDMOC established access through the superior vena cava or the right common iliac vein. It was then navigated under magnetic actuation through the inferior vena cava to reach target locations, such as branches of the hepatic vein or renal vein (Fig. 7B). A 1000-mm-long MDMOC for vascular interventional therapy was specially designed and fabricated using a custom-built 3D multi-axial printer (Fig. 7C). The MDMOC features a round-shaped polymer head at its front end, which can reduce the risk of vascular wall injury during operation while preserving functional integrity.

The liver is a common metastatic site for various cancers (e.g., gastric, colorectal, and breast cancers), thus precise and efficient hepatic vein interventions hold significant clinical importance[60]. To demonstrate this capability, MDMOC entered the inferior vena cava, navigated to the confluence with the hepatic vein, and was subsequently into the hepatic vein branches under the guidance of an external magnetic field (Fig. 7D). Radiographic imaging revealed that MDMOC exhibited exceptional flexibility, enabling it to navigate through sharp angles (~70°) and reach target locations with high precision under magnetic actuation (Fig. 7E). In contrast, without the assistance of an actuating field, MDMOC struggled to traverse the complex curved pathways and frequently stalled at the confluence of the hepatic vein and inferior vena cava (Supplementary Movies 2 and 3). These results highlight superior navigation capabilities of MDMOC in complex vascular networks.

Renal vascular interventions serve as essential diagnostic and therapeutic strategies for renal vascular-related diseases, including renal cancer and renal function impairment. We further evaluated the ability of MDMOC to navigate into renal vein branches via the inferior vena cava under magnetic guidance (Fig. 7F). Without magnetic field assistance, MDMOC frequently stalled at the confluence of the renal vein and the inferior vena cava (Supplementary Movie 4). In contrast, MDMOC could reach the renal vein branches rapidly and precisely under magnetic guidance (Fig. 7G). The magnetic field-responsive deformation of MDMOC significantly enhanced navigation capability through complex vascular networks. Moreover, MDMOC also exhibited precise drug delivery capabilities. Specifically, MDMOC effectively injected iodinated contrast agents into renal vein branches, achieving full vascular system imaging within seconds while preserving vascular structural integrity and preventing drug extravasation. Consequently, MDMOC can facilitate targeted drug delivery under magnetic navigation, thereby reducing the risk of systemic side effects associated with drug administration. The introduction of MDMOC enhances precision and safety in interventional procedures, particularly for patients with

https://doi.org/10.1038/s41467-026-70529-6

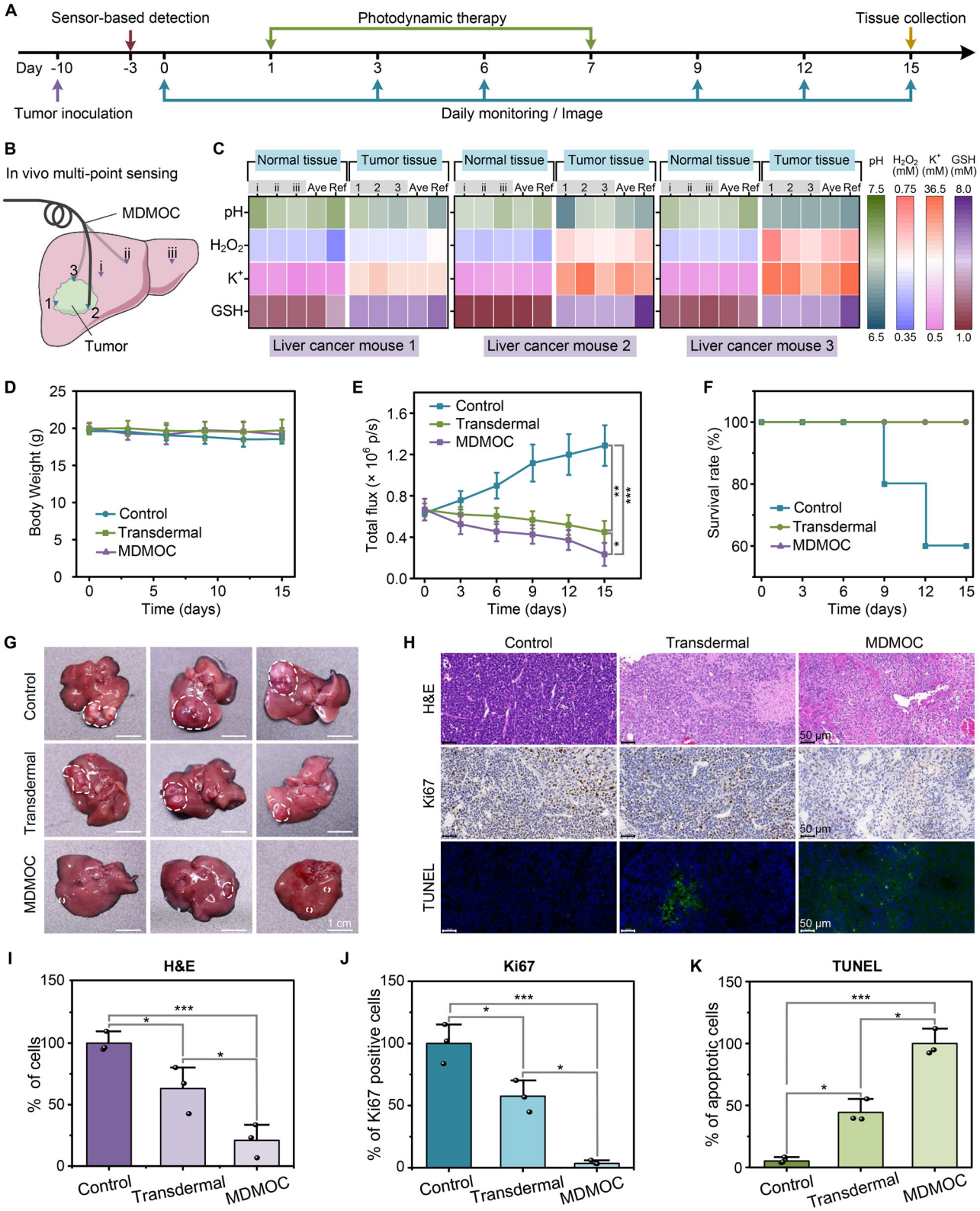

Fig. 6 | In vivo tumor diagnosis and therapy using MDMOC. A Schematic of tumor model establishment, treatment, and detection timeline. **B** Illustration of MDMOC detection in normal liver and tumor tissues. **C** Comparative analysis of detection results between normal and tumor tissues. **D** Body weight records during treatment. $n = 5$ animals per group. Data are shown as mean ± s.d. **E** Fluorescence intensity of orthotopic liver tumors under different treatments. Data are shown as mean ± s.d.; $n = 5$ animals per group. $P = 0.0013$ (Control vs Transdermal), $P = 0.00035$ (Control vs MDMOC), and $P = 0.032$ (Transdermal vs MDMOC). **F** Survival curves during the treatment period. **G** Optical images of mouse livers at the end of the treatment cycle. **H** Histological and immunohistochemical analyses of tumor tissues at the end of the treatment cycle, including H&E, Ki67, and TUNEL (green: apoptotic cells; blue: cell nuclei). **I**–**K** Quantification of H&E, Ki67, and TUNEL results. Data are shown as mean ± s.d.; $n = 3$ animals per group. Exact P values (Control vs Transdermal, Control vs MDMOC, Transdermal vs MDMOC): H&E (0.036, 0.00093, 0.034), Ki67 (0.0022, 0.00046, 0.0019), TUNEL (0.002, 0.0002, 0.0028).

https://doi.org/10.1038/s41467-026-70529-6

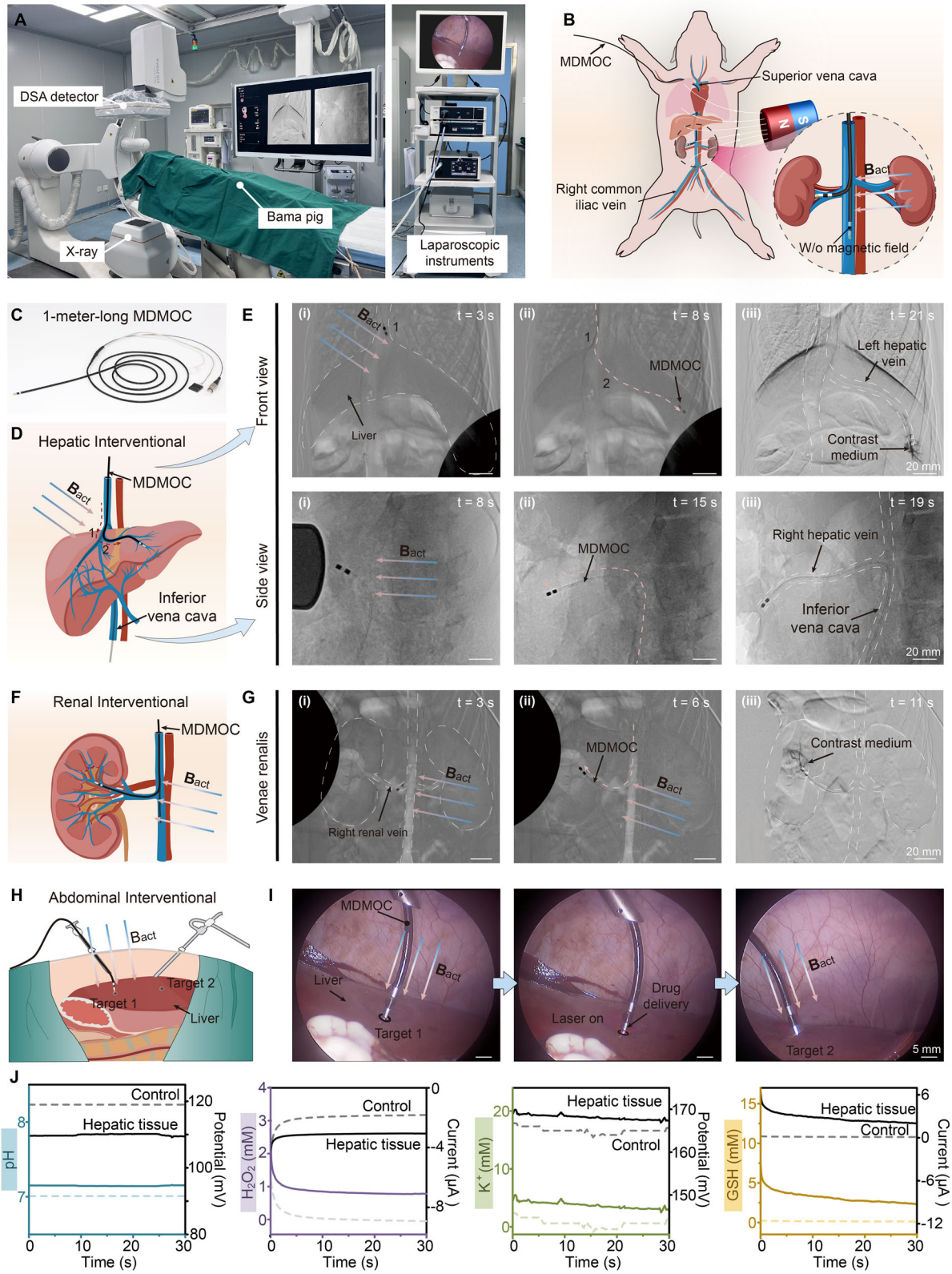

difficult-to-resect lesions, extensive metastases, or lesions located in hard-to-access regions, thereby providing critical support to improve treatment outcomes. The aforementioned vascular intervention experiments also demonstrated the exceptional compatibility of MDMOC with clinical imaging DSA system. MDMOC exhibited favorable radiopacity under X-ray imaging due to the incorporation of NdFeB magnets. This feature allowed real-time visualization of its tip trajectory, enabling clinicians to accurately assess its location and spatial orientation relative to surrounding vasculature, thereby streamlining surgical navigation.

Furthermore, we assessed the potential of MDMOC in abdominal interventional procedures. Under the guidance of endoscopic visual feedback and a magnetic field, MDMOC achieved precise localization of multiple lesions on the liver surface and demonstrated in situ

Fig. 7 | Demonstrations of minimally invasive interventional surgeries of MDMOC. A Schematic of the DSA and instrument used for in vivo interventional surgery in pig. **B** Illustration of vascular interventional procedures using MDMOC in a Bama pig. **C** Optical image of the 1000-mm-long MDMOC for intravascular interventional therapy. **D** Schematic representation of MDMOC navigating to the target hepatic vein location through two consecutive turns under magnetic field assistance. **E** Real-time imaging of MDMOC during vascular interventional procedures. The top panel shows the anterior view, where MDMOC is guided from the superior vena cava through the inferior vena cava to the left hepatic vein. The bottom panel presents the lateral view, where MDMOC is navigated from the right common iliac vein through the inferior vena cava to the right hepatic vein. $n = 3$ independent experiments. **F** Illustration of MDMOC performing renal vascular intervention. **G** Real-time imaging of MDMOC during renal vascular interventional procedures. $n = 3$ independent experiments. **H** Schematic of MDMOC performing abdominal interventional procedures. **I** Demonstration of effective puncture and therapeutic procedures under laparoscopic visualization. **J** In situ electrochemical sensing curves (potential/current) detected in the liver region and in the blank control region. Solid lines represent concentrations measured in the liver, while dashed lines represent concentrations from the control group.

diagnostic and therapeutic capabilities (Fig. 7H and Supplementary Movie 5). The results showed that MDMOC efficiently explored multiple lesion sites and successfully performed puncture operations under magnetic actuation for in situ diagnosis and treatment. Histological analysis of tissue obtained from the puncture sites via H&E staining revealed the formation of micro-channels at the targeted locations, providing solid evidence for subsequent histopathological evaluation and diagnosis (Supplementary Fig. 45). Even in the presence of significant liver motion caused by cardiac activity, MDMOC remained stably fixed at the target location (Fig. 7I). Leveraging its built-in drug delivery channel, MDMOC precisely administered therapeutic agents to each lesion site, directly targeting tumor tissues. This strategy not only enhanced treatment efficacy but also substantially minimized systemic side effects. Moreover, quantitative analysis of sensing signals using MDMOC was conducted based on standardized calibration curves established under in vitro conditions, with signals from standard solutions serving as controls. At the targeted liver locations, the apparent concentrations of H_2O_2, K^+, and GSH were approximately 0.81, 3.56, and 3.04 mM, respectively, with a pH value of 7.15. It should be noted that the in vivo H_2O_2 concentration was calculated using the in vitro H_2O_2 sensing curve as the calibration curve to convert the signal into concentration. Due to variations between the in vivo and in vitro environments, this signal-to-concentration conversion may induce some error in the actual value of the H_2O_2 concentration detected in vivo. Compared to the control group, the analyte concentrations detected on the liver surface were significantly elevated, further validating the high sensitivity and robust detection capability of MDMOC for in vivo target analytes (Fig. 7J). In situ detection results also confirmed the stability of MDMOC sensor signals with minimal fluctuation and negligible noise. Similarly, the in situ diagnostic and therapeutic performance of MDMOC was evaluated on the outer wall of the bladder in pigs (Supplementary Fig. 46 and Supplementary Movie 6). Therefore, MDMOC demonstrated unique advantages in multi-site diagnostics and therapeutics through continuous in situ electrochemical detection across multiple lesion regions. This enabled real-time spatial analysis of tumor biomarkers for comprehensive tumor diagnosis.

Discussion

In this work, we developed an MDMOC for minimally invasive surgery using 3D multi-axis printing technology. This innovative design integrates multiple functionalities, including magnetic navigation, in situ diagnosis, precise drug delivery, and PDT. By replacing conventional rigid wires with liquid metal-filled conductive channels, MDMOC achieves an ~8.2-fold increase in flexibility while maintaining excellent conductivity, enhancing maneuverability in complex surgical environments. Moreover, a hydrogel skin coated on the catheter surface effectively reduces friction, improving its navigability in complex anatomical environments. The synergistic integration of built-in permanent magnets and liquid metal channels enables real-time visualization of MDMOC under clinical CT imaging, allowing accurate localization and tracking relative to surrounding tissues. More importantly, the embedded electrochemical sensor array enables real-time monitoring of multiple tumor-associated biochemical markers (pH, H_2O_2, K^+, and GSH). Leveraging its superior magnetic navigation capability, MDMOC dynamically maps biomarker gradients across multiple sites within the tumor microenvironment, enabling accurate delineation of tumor boundaries. In a rabbit liver tumor model, multimodal fusion of biosensors significantly improved boundary detection accuracy and enhanced spatial resolution from millimeter to submillimeter scale, thereby refining the margins for targeted interventions. In an orthotopic liver cancer mouse model, MDMOC successfully detected four biochemical markers on the liver surface and markedly improved therapeutic efficacy through localized drug delivery combined with PDT. Further experiments in a Bama pig model confirmed that the MDMOC could precisely navigate to the targeted lesion site along the pre-set path, explore multiple lesions, perform in situ detection, and accurately deliver contrast agents.

Overall, the MDMOC demonstrated exceptional performance in detecting lesions, delineating boundaries, and providing real-time precise treatment for both single and multiple lesion tumors, showing potential to assist clinicians in performing high-precision tumor diagnosis and therapy in complex in vivo environments. Looking ahead, the sensing module of MDMOC could be extended beyond the current set of biochemical markers to include enzymatic activity detection, which may provide additional diagnostic dimensions for tumor characterization. Furthermore, expanding the detection panel to incorporate biomarkers more directly correlated with specific tumor types—such as certain proteases, metabolic enzymes, or nucleic acid-based indicators—could further enhance specificity and clinical relevance.

Methods

Materials

The CNT/isopropanol slurry, Ag/AgCl conductive inks, valinomycin, sodium tetraphenylborate (NaTPB), dioctyl sebacate (DOS), high-molecular weight polyvinyl chloride (PVC), sulfonated cobalt phthalocyanine (CoPcs), 3,4-ethylenedioxythiophene, benzophenone, chloroauric acid, Irgacure-2959, DMAA, SOSG, chlorin e6, poly(lactic-co-glycolic acid) (PLGA, acid terminated, L/G ratio = 75:25, Mw = 10,000–20,000), poly(vinyl alcohol) (PVA, 87–90% hydrolyzed, Mw = 70,000) were purchased from commercial sources and used without further purification.

Fabrication of MDMOC

Fabrication of arrow and round-shaped heads. An arrow-shaped head (length of 7 mm, base diameter of 2.5 mm) with seven angular edges for lowering tissue friction and a round-shaped head (length of 4.5 mm, base diameter of 2.5 mm) for eliminating vascular tissue damage were designed. The arrowhead and round-shaped heads were fabricated using a 3D microprinter (Nano Arch S140, BMF company, China).

3D printing of flexible multi-axial sheaths. The printing ink was prepared by mixing 0.03% alcohol-soluble aniline black with 99.97% PDMS (SE 1700, Dow Corning, USA). Multi-axial sheaths were coaxially printed in one step using a custom-developed coaxial printer with a

specific multi-core coaxial nozzle and subsequently cured at 70 °C for 1 h.

Modification of surface hydrogel on multi-axial sheath. The multi-axial sheath was immersed in a 10% benzophenone ethanol solution for 5 min, dried at room temperature for 2 h. It was further immersed in a solution containing 1% Irgacure-2959 and 20% DMAA for UV cross-linking for 1 h. Finally, the sheath was washed to remove any unreacted components.

Preparation of biosensors. The base electrode with a length of 3 mm was polished to diameter of 0.1 mm and subsequently treated with plasma cleaning. For the reference electrode, it was immersed in Ag/AgCl conductive ink for 10 cycles to form a conductive layer, then dried at room temperature for 12 h. For the counter electrode and H_2O_2 working electrode, Pt nanoparticles were electroplated on their surfaces by immersing them in a platinum sulfite solution using a multi-step current method, then dried at room temperature for 12 h. For the pH working electrode, it was immersed in a solution of 0.1 M aniline and 1 M HCl. Cyclic voltammetry was then performed to form a polyaniline layer on its surface, after which the electrode was dried at room temperature for 12 h. For the K^+ working electrode, a CNT/isopropyl alcohol slurry was firstly coated on the base electrode, and then immersed in a solution of valinomycin (2% w/w), NaTPB (0.5% w/w), PVC (32.7% w/w), and DOS (64.7% w/w) dissolved in cyclohexanone, and a K^+-selective permeable membrane was formed. For the GSH working electrode, the base electrode was immersed 10 cycles in a GSH-sensitive slurry made by dissolving 5 mg CNT@CPEDOT in 500 μL isopropanol. CNT@CPEDOT was synthesized by dispersing 2 mg CNT in 30 mL isopropanol, adding 500 μL EDOT, 5 mL of 10 mM CoPcs, and 2 mL of 25 mM $HAuCl_4$, then centrifuging, washing, and drying the precipitate.

Assembly of MDMOC. The permanent magnet was firstly coated with an 80 μm PDMS layer. The magnet, polymer head, electrodes, and hydrogel skin-modified sheaths were bonded and coated with light-curing resin, and the head section of MDMOC was fabricated. Subsequently, the optical fiber, coaxial sheath, catheter, and wires were assembled as the body of MDMOC. Finally, the head and body of MDMOC were tightly bonded using light-curing resin. In parallel, adhesion strength analysis was conducted to further validate the robustness and reliability of the bonding interface.

Morphological characterization of MDMOC

The morphology and EDS of the MDMOC were analyzed using an SEM (Quanta 400 F, FEI, USA). Conductive connections between the electrode and liquid metal within MDMOC were observed using a Micro-CT (SkyScan 2211, Bruker, GER). The optical images of MDMOC were captured using a digital camera (EOS 5D, Canon, Japan). Electrode morphology was analyzed using an ultra-depth 3D microscope (VHX-7000, KEYENCE, Japan).

Magnetic, electric, optical properties, and drug delivery performance tests of MDMOC

The magnetic properties of MDMOC were systematically analyzed. Additionally, the deformability behavior of the MDMOC filled with air, liquid metals, and copper wires was investigated under an external magnetic field generated by a Helmholtz coil (WD-60, Changchun Yingpu Magnetic Technology Development Co., Ltd., China). The MDMOC deformation was also analyzed using finite element method in COMSOL Multiphysics 6.0 (COMSOL Inc., Sweden). MDMOC model was built by coupling the solid mechanics module with the current module. The deformation under magnetic actuation at each step involved an interactive calculation of the magnetic force, derived from the integration of the magnetic stress tensor generated by the actuating field **B** and magnetization profile **m**. Magnetic forces were computed using the magnetic field-no current module, while the deformation was calculated using the solid mechanics module. The final deformation of MDMOC was obtained through multi-step iterative calculations.

The magnetic navigation of MDMOC in multi-degree-of-freedom was investigated using self-developed 8-axis electromagnetic coil apparatus. The apparatus generates a 3D dynamic magnetic field **B** using 8 uniformly distributed electromagnetic coils in a spherical configuration. A stepper motor controls the advancement and retraction of MDMOC, while two industrial camera monitors its position in real-time for closed-loop control. The MDMOC head was disassembled to verify laser irradiation and electrical conductivity capabilities. MDMOC was magnetically actuated to irradiate the developing card along a pre-designed path with a 470 nm blue light via its optical fiber. The exposed electrodes were connected to the negative terminal of an external power supply, while the positive terminal to a custom PCB board. MDMOC activated LEDs at multiple sites under magnetic actuation.

The puncture performance of MDMOC was investigated using a universal testing machine (ZQ-990B, Dongguan ZhiQu Precision Instruments Co., Ltd., China). The MDMOC was gradually inserted into rat liver tissue with a loading displacement of 2 mm at a speed of 0.1 mm/s. A model drug (rhodamine B solution) was delivered using a peristaltic pump, and the fluid transport and potential leakage were systematically observed and analyzed under different bending angles to evaluate the drug delivery performance of the MDMOC.

In vitro electrochemical sensing tests

The electrochemical sensing performance of MDMOC was evaluated using an Electrochemical Workstation (CHI660E, Shanghai Chenghua Instrument Co., Ltd., China). The sensitivity, selectivity, reproducibility, and stability were tested systematically. For sensitivity, the pH and K^+ sensors measured potential signals at varying pH levels or K^+ concentrations using the open-circuit potential method. The H_2O_2 and GSH sensors recorded current signals at various concentrations under specific bias voltages (−0.5 V for the H_2O_2 sensor and 0.4 V for the GSH sensor). Selectivity was assessed by continuously adding different interferers and recording the potential or current signal changes. Reproducibility was studied by measuring the relative deviation of four sensors (five each) detecting the same solution with different working electrodes. For stability, Stability was tested by storing electrodes at 4 °C and periodically measuring their relative deviation from the initial signal (every 2 h for the first 12 h and then daily).

Ethics statement

The experimental protocol was approved by the Institutional Animal Care and Use Committees of Sun Yat-sen University (SYSU-IACUC-2024-B1615), South China Agricultural University (2025F901), Top BioTech Co., Ltd., Shenzhen (TOP-2PZ-GM250701), and Huanteng BioTech Co., Ltd., Guangzhou (B202409-7). All animals were handled in accordance with the guidelines for the care and use of laboratory animals provided by these institutions.

Animal experimental

Female BALB/c nude mice (Mus musculus, BALB/c substrain, immunodeficient, ~20 g, ~5 weeks old, Animal Center of Sun Yat-sen University, China) were used for diagnostic and therapeutic validation. Female New Zealand rabbits (Oryctolagus cuniculus, outbred, ~3 kg, Zhuhai Beston BioTech Co., Ltd., China) were used for tumor boundary detection experiment. Female Bama miniature pigs (Sus scrofa, Bama strain, ~35 kg, Huanteng BioTech Co., Ltd., Guangzhou, China) were used for minimally invasive surgery experiments.

In vivo tumor boundary mapping using MDMOC in a rabbit liver cancer model. Single-lesion, multi-lesion, and local-boundary liver cancer models were established in adult New Zealand rabbits. Preoperative anesthesia was induced via auricular vein injection of sodium pentobarbital (30 mg/kg), followed by intraoperative maintenance

with 1.5% isoflurane. Under assistance of laparoscopic observation and magnetic navigation, a 2.5 mm-diameter MDMOC was inserted through a minimally invasive incision into both the tumor site and adjacent normal liver tissue. The closed-loop workflow, from tumor detection using biosensors to drug delivery and PDT, was performed. In multi-point detection mode (step size: 5 mm), in situ signals from four electrochemical sensors (pH, H_2O_2, K^+, and GSH) were collected sequentially, with spatial coordinates documented. Using calibration curves, the signals were converted into concentration maps to generate 2D heatmaps. The concentration heatmap was generated by mapping the measured concentrations at discrete sampling points to their spatial coordinates, followed by spatial interpolation (via Origin 2022) to estimate the concentration distribution over the entire region. These heatmaps were compared with ultrasound imaging and H&E histopathology to evaluate the accuracy of single- and multimodal sensing in detection of tumor boundaries.

In vivo theranostic of MDMOC in BALB/c nude mice. A PBS suspension of 1 million HepG2-luc cells (human, male donor, Catalog Number: STCC00037P, Wuhan Servicebio Technology Co., Ltd., Wuhan, China) was injected into the mouse liver to establish an orthotopic liver tumor model. Prior to tumor inoculation, mice were acclimated for 7 days in a barrier facility under a 12-h light/12-h dark cycle, with controlled ambient temperature (22 ± 2 °C) and humidity (50–60%). The tumor in the liver was observed using Fluorescence imaging. Tumor-bearing mice were anesthetized with 1.5% isoflurane gas. The MDMOC was inserted into the liver tumor or normal liver tissue at three positions (distant, intermediate, and proximal to the tumor tissue), secured, and connected to an electrochemical workstation for testing. At the end of the experiment, tissue fluid from the experimental site was extracted and analyzed biochemically using a standard analyzer to determine reference concentrations. In the experimental group, the drug PLGA@Ce6 (5 mg/kg) was directly injected into the tumor tissue via MDMOC for the in situ treatment of mouse hepatocellular carcinoma. The tumor site was then irradiated with a laser (500 mW, 660 nm) for 5 min via MDMOC. In the control group, the tumor received laser irradiation 5 min after drug administration. In the control group, only laser irradiation was applied without any drug. Therapeutic effects were monitored using small animal live imaging, and the weight and survival of the mice were daily recorded.

Clinical surgery of MDMOC in Bama Pig. Bama pigs were fasted and deprived of water for 8 h before surgery. Atropine (0.04 mg/kg) was intramuscularly injected 15 min before anesthesia induction, followed by Sutaine (5 mg/kg) for anesthesia. After achieving optimal anesthesia depth, tracheal intubation and intravenous access were established. Magnetic navigation of MDMOC was driven by a permanent magnet. During vascular micro-interventional procedures, the anesthetized pig was placed supine on an X-ray surgical table, and a vascular sheath was inserted into the superior vena cava. The MDMOC was introduced via the superior vena cava, and vascular distribution was recorded by injecting a contrast agent. Intravascular motion images of the MDMOC were captured by DSA. Guided by an external magnetic field, the MDMOC reached the left hepatic and renal veins, where contrast agents were injected to simulate drug delivery. A vascular sheath was also placed in the right common iliac vein, and the MDMOC was navigated through the inferior vena cava to the right hepatic vein under magnetic actuation.

For abdominal interventions, two minimally invasive incisions were made in the abdominal wall for inserting endoscopic trocars and MDMOC. The abdominal cavity was continuously insufflated through a trocar for endoscopic visualization, and the MDMOC was magnetically manipulated under endoscopic guidance. Under magnetic navigation, the MDMOC punctured the target site in the liver, enabling in situ electrochemical detection. To simulate in situ drug delivery, a Rhodamine B solution was injected, followed by laser irradiation. Similarly, drug delivery and laser treatment were demonstrated on the bladder's outer wall under laparoscopic visualization. At the conclusion of the experiment, liver tissue punctured by the MDMOC was collected and subjected to HE staining for analysis.

Safety studies

To assess the cytotoxicity of MDMOC, CCK-8 method and live/dead cell staining were used to evaluate cell activity in HepG2 and LO-2 cells obtained from Wuhan Servicebio Technology Co., Ltd., Wuhan, China. After 3 days of incubation with MDMOC extract, absorbance was measured at 450 nm using a microplate reader (Multiskan FC, Thermo Scientific, China), and stained cells were captured using a fluorescence microscope (Nikon ECLIPSE Ti). At the end of the treatment, all mice were euthanized. Their livers and major organs were collected, and photographs were taken to scale. The tumors and major organs were immobilized in 4% (v/v) paraformaldehyde solution, embedded in paraffin wax, and dissected to 4 μm thickness for histological analysis with H&E staining. Immunohistochemical staining was performed using Anti-Ki67 Mouse Monoclonal Antibody (Clone 6D12B2, Servicebio, Cat. No. GB121141-100) at 1:200 dilution as a marker for cell proliferation. The apoptosis of tumor cells was detected by dUTP notch end labeling (TUNEL) mediated by terminal deoxynucleotide transferase, and histopathological evaluation was performed to study the safety and efficacy of MDMOC therapy.

Statistical analysis

Data are presented as mean ± standard deviation (SD). Comparisons between two groups were performed using a two-tailed Student's t-test. Statistical significance was classified as $^*P < 0.05$ (significant), $^{**}P < 0.01$ (highly significant), and $^{***}P < 0.001$ (extremely significant).

Reporting summary

Further information on research design is available in the Nature Portfolio Reporting Summary linked to this article.

Data availability

All data supporting the findings of this study are available within the article and its supplementary files. Any additional requests for information can be directed to, and will be fulfilled by, the corresponding authors. Source data are provided with this paper.

References

1. Bray, F. et al. Global cancer statistics 2022: GLOBOCAN estimates of incidence and mortality worldwide for 36 cancers in 185 countries. *CA Cancer J. Clin.* **74**, 229–263 (2024).
2. Alix-Panabières, C. & Pantel, K. Advances in liquid biopsy: from exploration to practical application. *Cancer Cell* **43**, 161–165 (2024).
3. Gerlinger, M. et al. Intratumor heterogeneity and branched evolution revealed by multiregion sequencing. *N. Engl. J. Med.* **366**, 883–892 (2012).
4. Schmelz, K. et al. Spatial and temporal intratumour heterogeneity has potential consequences for single biopsy-based neuroblastoma treatment decisions. *Nat. Commun.* **12**, 6804 (2021).
5. Ogrinc, N. et al. Cancer Surgery 2.0: guidance by real-time molecular technologies. *Trends Mol. Med.* **27**, 602–615 (2021).
6. Cheng, H. et al. Illuminating the future of precision cancer surgery with fluorescence imaging and artificial intelligence convergence. *npj Precis. Oncol.* **8**, 196 (2024).
7. Hiller, J. G. et al. Perioperative events influence cancer recurrence risk after surgery. *Nat. Rev. Clin. Oncol.* **15**, 205–218 (2018).
8. Ruysscher, D. D. et al. Radiotherapy toxicity. *Nat. Rev. Dis. Primers* **5**, 13 (2019).
9. Zhong, L. et al. Small molecules in targeted cancer therapy: advances, challenges, and future perspectives. *Signal Transduct. Target.Ther.* **6**, 201 (2021).

10. Mitchell, M. J. et al. Engineering precision nanoparticles for drug delivery. *Nat. Rev. Drug Discov.* **20**, 101–124 (2021).
11. Liu, C. et al. Cation-π interaction-mediated tumour drug delivery for deep intratumoral penetration and treatment. *Adv. Funct. Mater.* **32**, 2205043 (2022).
12. Liang, X. et al. Inherent tumor microenvironment-reversing hydrogels: potentiating molecular therapy efficacy against drug-resistant tumors. *Adv. Funct. Mater.* **34**, 2314772 (2024).
13. Kimura, Y. et al. Expanding the role of interventional oncology for advancing precision immunotherapy of solid tumors. *Mol. Ther. Oncolytics* **24**, 194–204 (2022).
14. Franklin, J. M. et al. A. Clinical trials of interventional oncology—moving from efficacy to outcomes. *Nat. Rev. Clin. Oncol.* **12**, 93–104 (2015).
15. McNamara, D. A. et al. Comparison of radiation exposure among interventional echocardiographers, interventional cardiologists, and sonographers during percutaneous structural heart interventions. *JAMA Netw. Open* **5**, e2220597 (2022).
16. Zhang, T. et al. Impact of operator experience on left atrial appendage occlusion outcomes. *JACC: Clin. Electrophysiol.* **10**, 2461–2470 (2024).
17. Zhou, C. et al. Ferromagnetic soft catheter robots for minimally invasive bioprinting. *Nat. Commun.* **12**, 5072 (2021).
18. Zhang, T. et al. Millimeter-scale soft continuum robots for large-angle and high-precision manipulation by hybrid actuation. *Adv. Intell. Syst.* **3**, 2000189 (2021).
19. Zhang, T. et al. Sub-millimeter fiberscopic robot with integrated maneuvering, imaging, and biomedical operation abilities. *Nat. Commun.* **15**, 10874 (2024).
20. Yang, J. et al. Magnetically actuated multimodal bioelectronic catheter for minimally invasive surgery and sensing. *Nat. Mater.* **24**, 2019–2031 (2025).
21. Zhang, Y. et al. Coaxially printed magnetic mechanical electrical hybrid structures with actuation and sensing functionalities. *Nat. Commun.* **14**, 4428 (2023).
22. Rafii-Tari, H. et al. Current and emerging robot-assisted endovascular catheterization technologies: a review. *Ann. Biomed. Eng.* **42**, 697–715 (2014).
23. Patel, T. M. et al. Comparison of robotic percutaneous coronary intervention with traditional percutaneous coronary intervention: a propensity score-matched analysis of a large cohort. *Circ. Cardiovasc. Interv.* **13**, e008888 (2020).
24. Hwang, J. et al. An electromagnetically controllable microrobotic interventional system for targeted, real-time cardiovascular intervention. *Adv. Healthc. Mater.* **11**, 2102529 (2022).
25. Kim, Y. et al. Telerobotic neurovascular interventions with magnetic manipulation. *Sci. Robot.* **7**, eabg9907 (2022).
26. Yang, Z. et al. Magnetically actuated continuum medical robots: a review. *Adv. Intell. Syst.* **5**, 2200416 (2023).
27. Kim, Y. et al. Ferromagnetic soft continuum robots. *Sci. Robot.* **4**, eaax7329 (2019).
28. Lee, W. et al. Steering, tunneling, and stent delivery of a multifunctional magnetic catheter robot to treat occlusive vascular disease. *IEEE Trans. Ind. Electron.* **68**, 391–400 (2021).
29. Dreyfus, R. et al. Dexterous helical magnetic robot for improved endovascular access. *Sci. Robot.* **9**, eadh0298 (2024).
30. Piskarev, Y. et al. A variable stiffness magnetic catheter made of a conductive phase-change polymer for minimally invasive surgery. *Adv. Funct. Mater.* **32**, 2107662 (2022).
31. Piskarev, Y. et al. Fast-response variable-stiffness magnetic catheters for minimally invasive surgery. *Adv. Sci.* **11**, 2305537 (2024).
32. Mao, L. et al. Magnetic steering continuum robot for transluminal procedures with programmable shape and functionalities. *Nat. Commun.* **15**, 3759 (2024).
33. Yang, P. et al. A cooperative and multifunctional magnetic continuum robot for noninteractive access, dexterous navigation, and versatile manipulation. *Adv. Funct. Mater.* **35**, 2412543 (2024).
34. Edelmann, J. et al. Estimation-based control of a magnetic endoscope without device localization. *J. Med. Robot. Res.* **3**, 1850002 (2018).
35. Slawinski, P. R. et al. Autonomously controlled magnetic flexible endoscope for colon exploration. *Gastroenterology* **154**, 1577–1579.e1 (2018).
36. Martin, J. W. et al. Enabling the future of colonoscopy with intelligent and autonomous magnetic manipulation. *Nat. Mach. Intell.* **2**, 595–606 (2020).
37. Lee, M. et al. Confocal laser endomicroscope with distal MEMS scanner for real-time histopathology. *Sci. Rep.* **12**, 20155 (2022).
38. Li, Y. et al. Design and preliminary evaluation of an electromagnetically actuated soft-tethered colonoscope. *IEEE Trans. Med. Robot. Bionics* **3**, 402–413 (2021).
39. Yuan, S. et al. Motor-free telerobotic endomicroscopy for steerable and programmable imaging in complex curved and localized areas. *Nat. Commun.* **15**, 7680 (2024).
40. Vodnala, S. K. et al. T cell stemness and dysfunction in tumors are triggered by a common mechanism. *Science* **363**, eaau0135 (2019).
41. Chao, Y. & Liu, Z. Biomaterials tools to modulate the tumour microenvironment in immunotherapy. *Nat. Rev. Bioeng.* **1**, 125–138 (2023).
42. Hori, S. S. et al. Cancer diagnostics: on-target probes for early detection. *Nat. Biomed. Eng.* **1**, 0062 (2017).
43. Chu, Z. et al. Recent advances on modulation of H_2O_2 in tumor microenvironment for enhanced cancer therapeutic efficacy. *Coord. Chem. Rev.* **481**, 215049 (2023).
44. Peng, S. et al. Tumor-microenvironment-responsive nanomedicine for enhanced cancer immunotherapy. *Adv. Sci.* **9**, 2103836 (2022).
45. Wang, L. et al. Hard-magnetic elastica. *J. Mech. Phys. Solids* **142**, 104045 (2020).
46. Chen, Z. et al. Additive manufacturing of honeybee-inspired microneedle for easy skin insertion and difficult removal. *ACS Appl. Mater. Interfaces* **10**, 29338–29346 (2018).
47. Ling, J. et al. Effect of honeybee stinger and its microstructured barbs on insertion and pull force. *J. Mech. Behav. Biomed. Mater.* **68**, 173–179 (2017).
48. Gong, X. et al. Polymer hydrogel-based multifunctional theranostics for managing diabetic wounds. *Adv. Funct. Mater.* **34**, 2315564 (2024).
49. Kim, H. et al. Bioelectronic sutures with electrochemical pH-sensing for long-term monitoring of the wound healing progress. *Adv. Funct. Mater.* **34**, 2402501 (2024).
50. Jin, Q. et al. Reduced graphene oxide nanohybrid-assembled microneedles as mini-invasive electrodes for real-time transdermal biosensing. *Small* **15**, 1804298 (2019).
51. Lu, Z. et al. Novel flexible bifunctional amperometric biosensor based on laser engraved porous graphene array electrodes: highly sensitive electrochemical determination of hydrogen peroxide and glucose. *J. Hazard. Mater.* **402**, 123774 (2021).
52. Yang, J. et al. Masticatory system-inspired microneedle theranostic platform for intelligent and precise diabetic management. *Sci. Adv.* **8**, eabo6900 (2022).
53. Huang, S. et al. Petromyzontidae-biomimetic multimodal microneedles-integrated bioelectronic catheters for theranostic endoscopic surgery. *Adv. Funct. Mater.* **33**, 2214485 (2023).
54. Wu, W.-T. et al. Versatile construction of biomimetic nanosensors for electrochemical monitoring of intracellular glutathione. *Angew. Chem. Int. Ed.* **61**, e202115820 (2022).
55. Jiao, Y. et al. Fast antioxidation kinetics of glutathione intracellularly monitored by a dual-wire nanosensor. *Angew. Chem. Int. Ed.* **62**, e202313612 (2023).

56. Feng, L. et al. The acidic tumor microenvironment: a target for smart cancer nano-theranostics. *Natl. Sci. Rev.* **5**, 269–286 (2018).
57. Li, X. et al. Clinical development and potential of photothermal and photodynamic therapies for cancer. *Nat. Rev. Clin. Oncol.* **17**, 657–674 (2020).
58. Li, G. et al. Advances in smart nanotechnology-supported photodynamic therapy for cancer. *Cell Death Discov.* **10**, 466 (2024).
59. Chen, Y. et al. Self-reporting photodynamic nanobody conjugate for precise and sustainable large-volume tumor treatment. *Nat. Commun.* **15**, 6935 (2024).
60. Dong, D. et al. Cellular and molecular mechanisms of gastrointestinal cancer liver metastases and drug resistance. *Drug Resist. Updates* **77**, 101125 (2024).

Acknowledgements

This work was supported by the National Natural Science Foundation of China (Grant No. T2225010; Grant Nos. 52305442, 52305458, 52175446, 52405329, 52575553, and 32171399), the Shenzhen Science and Technology Plan Project (Grant Nos. JCYJ20220818102201003, KCXFZ20230731094500001, and JCYJ20220818102201002), and the Guangdong Basic and Applied Basic Research Foundation (Grant No. 2025A1515010188).

Author contributions

L.J., X.X., and S.W. conceived and designed the project. L.J. and F.C. wrote the manuscript. L.J. and X.X. directed the research and provided recommendations for this work. F.C. conducted most of the experiments, analyzed the data, and completed the manuscript. X.L. assisted with the theoretical analysis and animal experiments. Yuanxi Zhang and Ying Zheng carried out theoretical calculation analysis and device design. J.Y. helped conduct animal experiments. T.W., K.Z., and W.C. data analysis, reference, and graph preparation. Y.L., X.G., and H.W. contributed to in vivo experiments and data collection. All authors discuss the results and comment on the manuscript.

Competing interests

The authors declare no competing interests.

Additional information

Supplementary information The online version contains supplementary material available at https://doi.org/10.1038/s41467-026-70529-6.

Correspondence and requests for materials should be addressed to Shuo Wu, Xi Xie or Lelun Jiang.

Peer review information *Nature Communications* thanks Molto Pallares and the other, anonymous, reviewer(s) for their contribution to the peer review of this work. A peer review file is available.